

Article

Electromagnetic and Thermal Analysis of a Permanent Magnet Motor Considering the Effect of Articulated Robot Link

Phuong Thi Luu ^{1,2}, Ji-Young Lee ^{2,3,*} , Ji-Heon Lee ³ and Jung-Woo Park ³

¹ R&D Center, Higen Motor Co., Ltd., Changwon 51555, Korea; tpluu@higenmotor.com

² Energy and Power Conversion Engineering, University of Science & Technology, Daejeon 34113, Korea

³ Electric Machines and Drives Research Center, Korea Electrotechnology Research Institute, Changwon 51543, Korea; ljh0524@keri.re.kr (J.-H.L.); jwpark@keri.re.kr (J.-W.P.)

* Correspondence: jylee@keri.re.kr; Tel.: +82-55-280-14-16

Received: 2 April 2020; Accepted: 19 June 2020; Published: 23 June 2020



Abstract: This paper presents the electromagnetic and thermal characteristics of a permanent magnet synchronous motor (PMSM) in a joint actuator which is used for articulated robot application. In an attempt to design a compact PMSM for the articulated robot, robot link should be taken into consideration during the motor design process as it can reduce the temperature distribution on motor, thus reducing the volume of the motor. A lumped-parameter thermal model of PMSM with and without a link is proposed considering the core loss, copper loss, and mechanical loss as heat sources. The electromagnetic and thermal analysis results are well confirmed by the experiment in a 400 W 20-pole/24-slot PMSM. The experiment results show that the robot link helps to reduce the motor end-winding temperature by about 40%, and this leads to an increase in power density of the motor.

Keywords: articulated robot link; electromagnetic field; permanent magnet synchronous machine; thermal problem

1. Introduction

Permanent magnet synchronous machines (PMSM) are preferably used for various applications which require high torque and power density in a limited space, like electric vehicles and robots [1]. There are several approaches to increase the power density of a PM motor, such as optimizing the geometric shape of either the stator or rotor [2,3], using Halbach Array PM type [4], or using soft magnetic alloy material for the stator core [5]. In general, to obtain the maximum power density of the motor, we need to consider both electromagnetic and thermal characteristics in the motor design process.

In PMSM, the operation must be done under the proper temperature to avoid the possibility of magnet demagnetization and to maintain a long insulation life. This is because the temperature rise affects the motor performance. Therefore, an accurate and reliable thermal prediction method is very important in the motor design stage. There are two common thermal analysis methods for electrical machines, including the analytical lumped-parameter-network method (LPTN) [6–13] and the numerical methods, like computational fluid dynamics (CFD) and the finite element method (FEM) [14–19]. The numerical methods are commonly used in thermal analysis with high accuracy. However, they have a huge disadvantage, which is that they are extremely time-consuming. LPTN is less time consuming and relatively less accurate, but it is a way to increase accuracy by thermal coefficients determined empirically by the database. Therefore, LPTN has proved to be advantageous as a fast and accurate method of heat calculation on numerous machine types [6–13].

In this paper, the electromagnetic and thermal characteristics of a PMSM are investigated considering the effect of the robot link. The robot link can significantly reduce the temperature of the motor, so it plays an important role in increasing the power density of the motor at the same operating speed. However, there have been few previous studies on the effectiveness of robotic links in the motor design process.

This paper is organized into the following sections: Section 2 briefly describes the motor design process and motor specifications. Section 3 focuses on the electromagnetic analysis as well as thermal analysis method. The two-dimensional (2D) FEM is used for magnetic calculation and the LPTN method is used to solve the thermal problem in this study. Motor prototype and experiment are shown in Section 4, and Section 5 provides the conclusions.

2. Designed Model

Figure 1 shows the structure of the articulated robot and its components, including links and smart actuator modules. The link is connected directly to the smart actuator module, which includes an electric motor, and also served as a cooling part for the motor. To investigate the effect of the robot link on the motor temperature, an equivalent link (Link_eq) of the same length and thickness as the original robot link was used for analysis and testing. Simplified equivalent links are easy to produce for test as well as thermal analysis modeling.

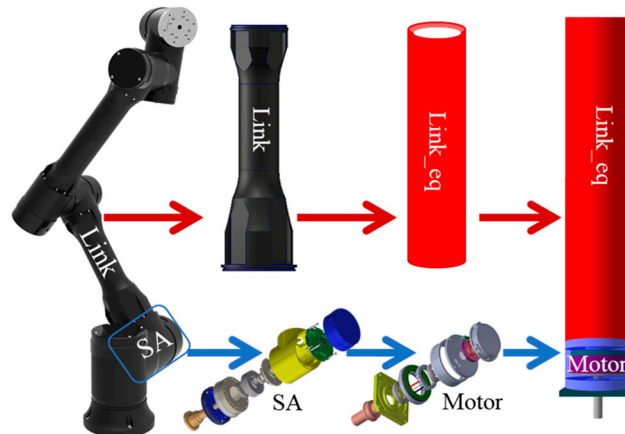


Figure 1. An articulated robot structure, including links and smart actuators (SA).

PMSM with 20-pole and 24-slot concentrated winding was adopted to use in smart actuator modules. As shown in Figure 2, some design variables including (1) tooth thickness, (2) stator yoke thickness, (3) stator inner diameter, (4) slot opening width, and (5) permanent magnet offset, which is the distance between the center of the motor and the center of the PM arc, were chosen for optimum design to obtain maximum efficiency and minimum cogging torque. Through the optimum design process, by using central composite design (CCD) and response surface methodology (RSM), a final model was chosen, and its main specifications are listed in Table 1. Besides, in order to maximize the power density of the motor, the segmented-stator core structure was used as it can increase the fill factor and decrease the cogging torque and torque ripple [14,20]. In terms of thermal design objective, the difference between temperature distributed on the end-winding and ambient temperature (ΔT) should be less than $55\text{ }^{\circ}\text{C}$ to prevent injury to humans caused by touching a hot surface when they work with articulated robots.

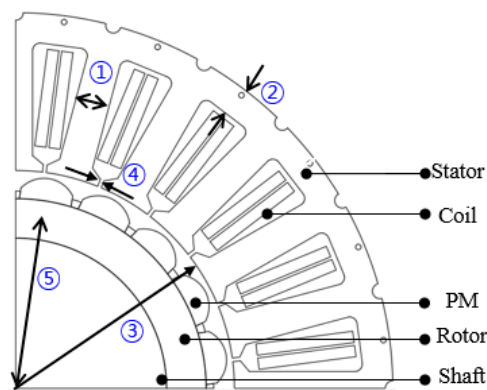


Figure 2. Design variables for optimum design by using central composite design (CCD) and response surface methodology (RSM).

Table 1. Specifications of the designed model.

Parameter	Value
Number of slots/poles	20/24
Rated Power	400 W
Stator Outer Diameter	100 mm
Air gap length	0.75 mm
Axial Length	25 mm
Cooling Type	Natural Cooling

3. Electromagnetic and Thermal Investigation

3.1. Analysis Assumptions

The analysis process involves two steps. The first step is electromagnetic analysis. The second stage is thermal analysis, where the loss data from the first stage is used as a heat source in the second stage. The following assumptions were used during the simulation:

- (1) The electromagnetic analysis is implemented at 80 °C. At that temperature, the residual magnetic flux density of PMs material is 1.24 Tesla.
- (2) The robot link is only considered in thermal analysis, not in electromagnetic analysis.
- (3) The force convection is considered in the air gap due to rotor rotation and free convection is considered in the outer housing.
- (4) Ambient temperature and initial temperature of the motor are set to 17 °C.

3.2. Electromagnetic Analysis

Electromagnetic characteristics of the designed motor were analyzed through 2D FEM Analysis software. A 1/4 periodical model was used in the analysis instead of a full model to save time. In the analytical model, the stator and rotor cores are made of laminated steel material (35PN440), which has a saturated point at 2 Tesla. As shown in Figure 3, the magnetic flux density distribution in the stator and rotor cores at the operating point is less than 1.8 Tesla, which does not exceed the saturated point of the core material.

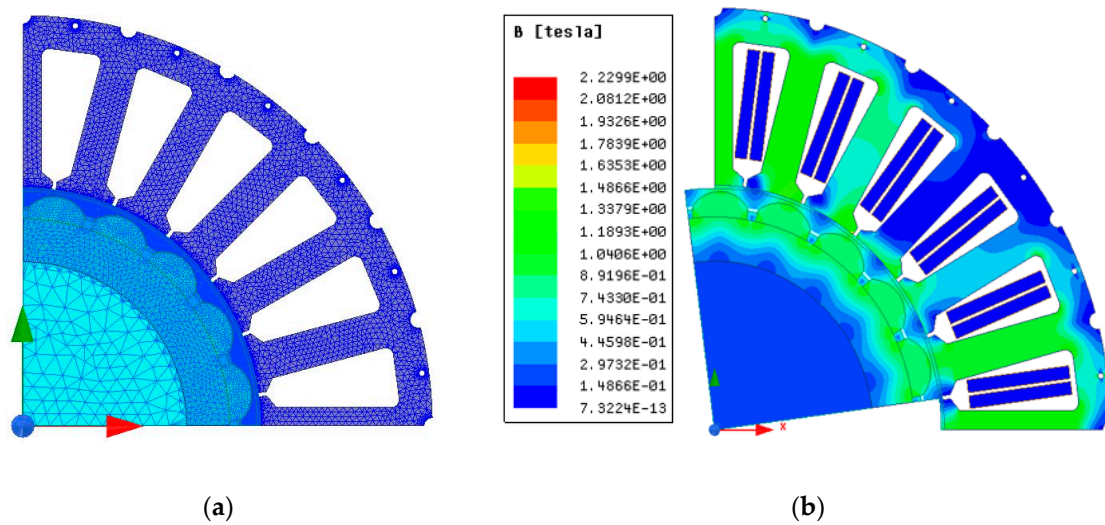


Figure 3. (a) Meshes of the analysis model, and (b) flux density distribution on the motor at the rated condition.

Motor losses considered in this study include core loss in the stator and rotor cores, copper loss in the winding, and mechanical loss, which is obtained by the measurement at the no-load condition. The copper loss per phase is derived from the phase current and winding resistance, while the core loss in the rotor and stator core depends on the flux density and frequency. Reference [21] presented the method of calculating core loss, which takes into account the harmonic effect of the magnetic flux density waveform on the core loss. The brief process is: (1) the magnetic flux density waveforms at each element of the meshed analysis model are calculated by FEM, (2) magnetic flux density waveforms are analyzed into frequency domain by using the Discrete Fourier Transforms (DFT), (3) the core losses at each element are calculated from the summation of the losses according to frequencies using DFT results and core loss curve, and (4) the total core loss is obtained by the summation of the core losses in all elements. This method is quite precise but complex. For this application, we use the simple method of calculating core loss considering the sinusoidal induction waveform, whereby it is calculated by Equation (1). Its accuracy has been proven based on the comparison of efficiency between test and analysis results in Reference [8].

$$p_i = k_h f B_m^2 + k_c f^2 B_m^2 + k_e f^{1.5} B_m^{1.5}, \quad (1)$$

where B_m is the peak flux density, f is the frequency, and coefficients k_h , k_c , and k_e can be obtained from the curve fitting of the measured loss data.

The performance and calculated losses of the designed motor are shown in Table 2. The cogging torque is less than 1% as compared to the rated torque, thus it satisfies the design requirement. The efficiency in the analysis is calculated by $P_{out}/(P_{out} + P_c + P_i + P_m)$, where P_{out} stands for the output power, P_c is the copper loss, and P_m is the mechanical loss. In this study, the mechanical loss is assumed to be 5% of the output power. The loss data obtained from the electromagnetic analysis is used as heat sources in the thermal analysis.

Table 2. Specifications of the designed model.

Motor Performance			
Current Density (Arms/mm ²)	Line Back Electromotive Force at 3200 rpm (Vrms)	Cogging Torque (mNm)	Efficiency (%)
5.8	26.81	2.5	87.7
Loss Data at 80 °C (W)			
Stator core loss 24.6	Rotor core loss 0.33	Copper loss 11.27	

3.3. Thermal Analysis

The lumped-parameter thermal model of the motor with and without a link is proposed to investigate the effect of the robot link on motor temperature distribution. In the thermal problem solving process, several iterations are performed. In each iteration, the temperature-dependent convection and radiation heat transfer coefficients are calculated based on the prior estimate temperature. To solve the thermal problem network, all the conduction, radiation, and convection thermal resistances should be determined.

The thermal network of the motor without the link as well as important parameters like the convective heat transfer coefficient in the air gap and outer housing has been presented in Reference [8]. In order to consider the link effect, the thermal network takes heat transfer on conduction, convection, and radiation from the link to other parts into account, by adding the thermal resistance and conductance. The thermal analysis model of the motor with the link and the thermal network circuit of the link part are shown in Figure 4.

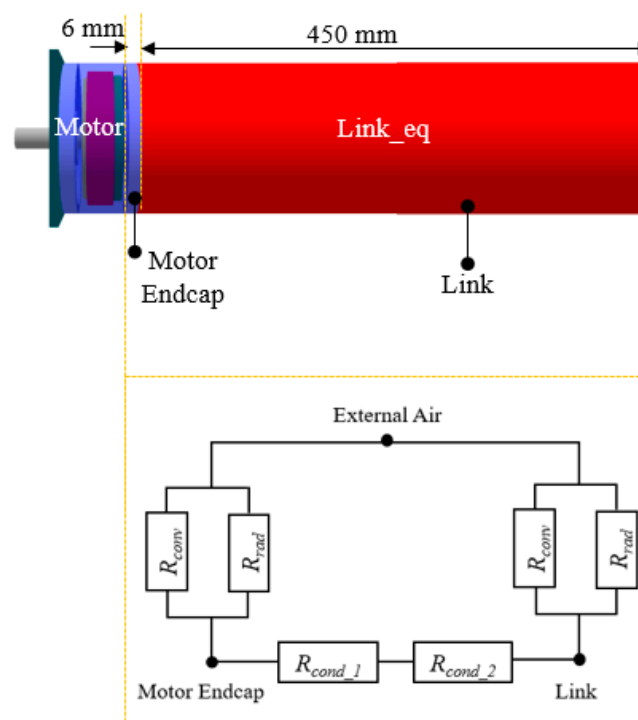


Figure 4. Thermal analysis model of the motor with the link (**upper**) and the thermal network circuit for the link part (**down**).

The resistance value for conductive heat transfer between the link and motor housing is calculated by Equation (2):

$$R_{cond_i} = \frac{l_i}{k_i A_i}, \quad (2)$$

where l_i (m) is the thickness of the motor part i , k (W/m °C) is the thermal conductivity of the material, and A_i is the contact area between two parts.

Since the motor is operated under natural cooling, the convective and radiative heat transfer between the externally exposed surface of the link and the ambient air cannot be neglected. The radiative resistance is obtained by Equation (3).

$$R_{rad} = \frac{1}{h_{rad} A} \quad (3)$$

$$h_{rad} = \sigma \varepsilon \frac{T_s^4 - T_a^4}{T_s - T_a}, \quad (4)$$

where h_{rad} is the radiation heat transfer coefficient and is calculated by Equation (4), σ is the Stefan-Boltzmann's constant (5.67×10^{-8} W·m⁻²·K⁻⁴), ε is the surface emissivity values for the link and is assumed to be 0.82 for the anodizing aluminum link, T_s is the surface temperature, and T_a is the ambient temperature.

The convective heat transfer coefficient (h_{conv}) between the external air and the link is referring to the empirical formula for the horizontal cylinder model, as presented in Reference [8]. The convective heat transfer resistance can be calculated by Equation (5):

$$R_{rconv} = \frac{1}{h_{conv} A} \quad (5)$$

The values for the heat transfer coefficient by radiation and convection of some important parts are shown in Table 3. Since the link is quite long, which is 450 mm in this study, it may cause inaccurate results in thermal analysis if we model the link as a single node. To examine the accuracy of thermal analysis results of the motor with the link, for each link's length value, we will compare the simulation results of two cases: Case 1, modeling the link as a single node, and Case 2, dividing the link into several nodes, where each node represents a part of the link with the length of 50 mm for each part. Figure 5 illustrates the thermal analysis results of DeltaT according to the change of the length of link. When L is shorter than 200 mm, there is small difference of DeltaT between Case 1 and Case 2. As L increases, DeltaT tends to increase after it reaches the minimum point at L = 400 mm in Case 1. This occurs because the conductive resistance between the motor endcap and the link increases as the length of the link increases, while the natural convective and radiative resistances decrease as the length of the link increases. These two competing effects result in a minimum of DeltaT. In Case 2, DeltaT continuously decreases when L increases. The difference of DeltaT between Case 1 and Case 2 at 450 mm of the link's length is about 13%. Therefore, for a long link, we should model the link as several nodes in the thermal network circuit to obtain a highly accurate result.

Table 3. Heat transfer coefficient of some important parts (unit: W/m²/°C).

	Convective Heat Transfer	Radiative Heat Transfer
Housing Outside	5.8	5.6
Air gap	49.01	-
Link	6.3	5.9

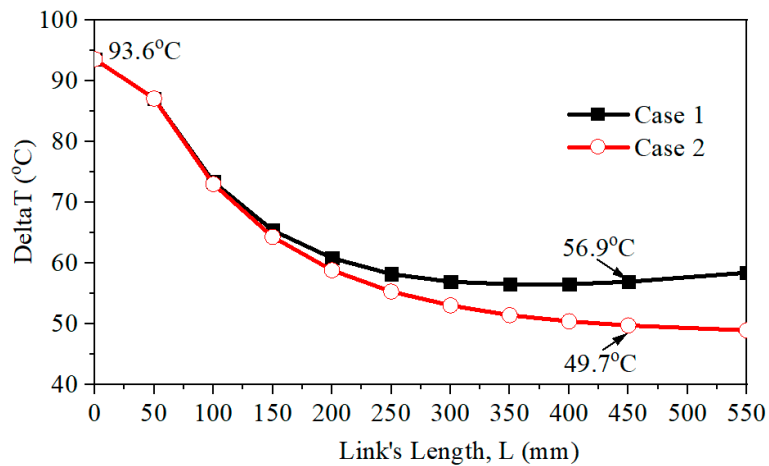


Figure 5. The analysis results of DeltaT according to the change of the link's length.

Also, it is clearly observed that the link has a big effect on the motor temperature, as it can reduce the end-winding temperature up to 40% in case of $L = 450$ mm.

4. Experimental Validation

To validate the analytical results, the proposed prototype with the main specifications presented in Table 1 was made and tested, as shown in Figure 6. The segmented cores were assembled after the coil was wound so it helps to significantly increase the slot fill factor compared to the motor with solid core. The experiment was implemented at the rated condition and an ambient temperature of around 17 °C, as shown in Figure 7. Links with equal lengths and thicknesses were used in the experiments instead of the original links to easily review the temperature effects of changes in link length.

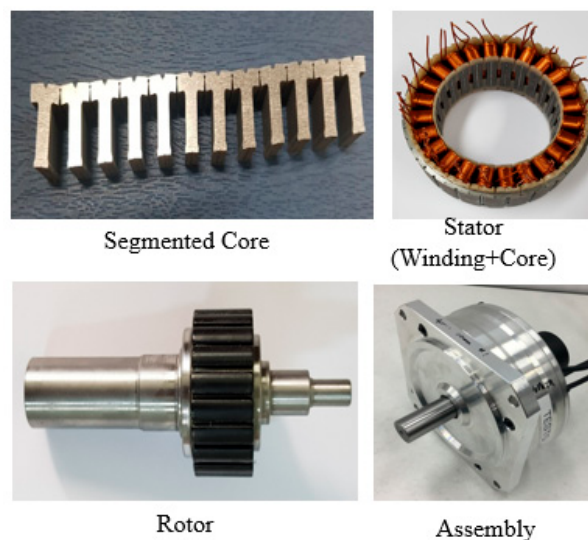


Figure 6. Proposed prototype.

Figure 8 shows the test results at the no-load condition of 3200 rpm. The measured value of the line-induced voltage (EMF) was 25.53 Vrms. The corresponding simulated back-EMF was 26.81 Vrms, showing under 5% difference with the measured data. The power loss at the no-load condition obtained from the experiment will be used for the heat sources in thermal analysis.

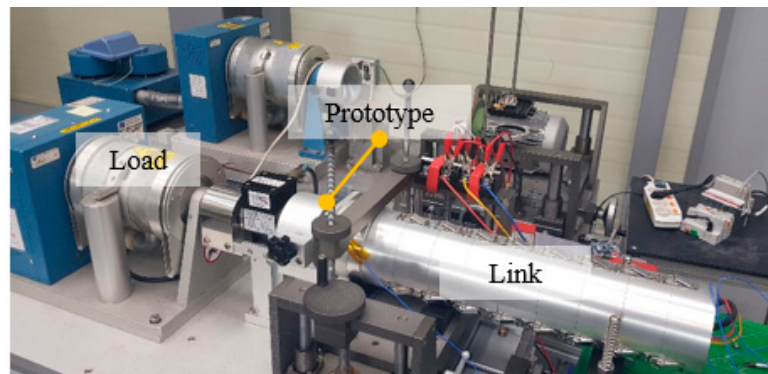


Figure 7. Experimental setup.

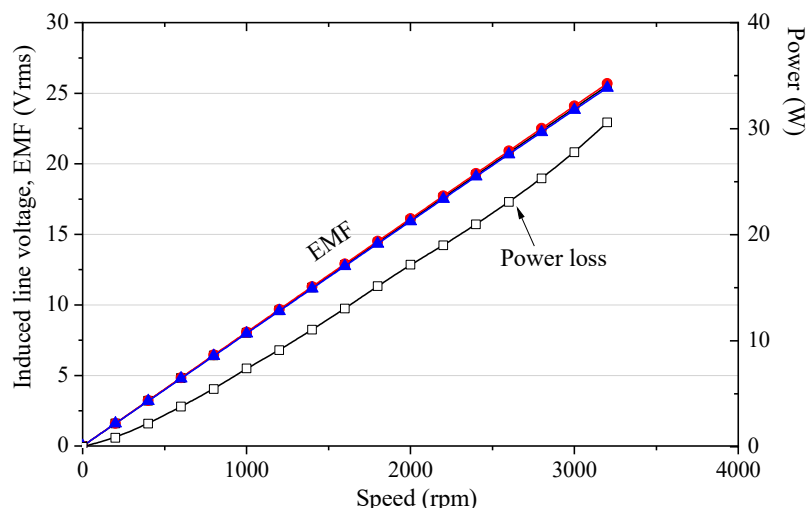


Figure 8. No-load test results according to speed variation.

The efficiency value was 88.5% in the experiment and it is in good agreement with the calculated value, which is 87.7%.

The thermal designed target is that ΔT must be less than $55\text{ }^{\circ}\text{C}$ to keep the high performance of the motor and prevent human injury. ΔT was checked by measuring the end-wing temperature through thermocouple. Two experiments for the motor with different lengths of the link were conducted to confirm the analysis results. Table 4 shows the comparison of ΔT between simulated and measured results. It is noteworthy that when we modeled the link as several nodes in the thermal network, the analysis result was closer to the experiment result compared to when we modeled the link as a single node for both values of the link’s length, as expected. At the length of link equal to 450 mm, ΔT was smaller than $55\text{ }^{\circ}\text{C}$ and it satisfies the design requirement.

Table 4. Comparison of ΔT between simulation and experiment (unit: $^{\circ}\text{C}$).

Link’s length, L = 300 mm		
Simulation_Case 1 56.8	Simulation_Case 2 52.5	Experiment 52.7
Link’s length, L = 450 mm		
Simulation_Case 1 56.9	Simulation_Case 2 49.7	Experiment 49.5

5. Conclusions

In an effort to make the high power density motor for the articulated robot, the effect of the robot link on the motor's working temperature has been considered in this study. In the case of the motor with the link, the end-winding temperature was reduced by 40% compared to the motor without the link. The thermal analysis using the LPTN method for the motor with the link with high accuracy by dividing the link into several nodes in the thermal network has been successfully verified by the experiment. These results are useful for the design and analysis of PMSM for robot applications, in which robot links can be considered as effective cooling parts to reduce the motor temperature, thus leading to an increase in the motor power density.

Author Contributions: Conceptualization, J.-Y.L. and P.T.L.; software, P.T.L.; validation, J.-H.L.; writing—P.T.L.; supervision, J.-Y.L.; project administration, J.-W.P. All authors have read and agreed to the published version of the manuscript.

Funding: This research received no external funding.

Acknowledgments: This Research was supported by Korea Electrotechnology Research Institute (KERI) Primary Research program through the National Research Council of Science and Technology (NST), funded by the Ministry of Science and ICT (MSIT) (No. 20A02032).

Conflicts of Interest: The authors declare no conflict of interest.

References

1. Lee, K.; Lee, J.; Woo, B.; Lee, J.; Lee, Y.; Ra, S. Modeling and control of a articulated robot arm with embedded joint actuators. In Proceedings of the 2018 International Conference on Information and Communication Technology Robotics (ICT-ROBOT), Busan, Korea, 8th September 2018; pp. 1–4.
2. Zhao, W.; Wang, X.; Gerada, C.; Zhang, H.; Liu, C.; Wang, Y. Multi-physics and multi-objective optimization of a high speed PMSM for high performance applications. *IEEE Trans. Magn.* **2018**, *54*, 1–5. [[CrossRef](#)]
3. Kong, Y.; Lin, M.; Jia, L. A novel high power density permanent-magnet synchronous machine with wide speed range. *IEEE Trans. Magn.* **2020**, *56*, 1–6. [[CrossRef](#)]
4. Li, L.; Zhang, J.; Zhang, C.; Yu, J. Research on electromagnetic and thermal issue of high-efficiency and high-power-density outer-rotor motor. *IEEE Trans. Appl. Super.* **2016**, *26*, 1–5. [[CrossRef](#)]
5. Fang, S.; Liu, H.; Wang, H.; Yang, H.; Lin, H. High power density pmsm with lightweight structure and high-performance soft magnetic alloy core. *IEEE Trans. Appl. Super.* **2019**, *29*, 1–5. [[CrossRef](#)]
6. Tong, W.; Sun, R.; Zhang, C.; Wu, S.; Tang, R. Loss and thermal analysis of a high-speed surface-mounted PMSM with amorphous metal stator core and titanium alloy rotor sleeve. *IEEE Trans. Magn.* **2019**, *55*, 1–4. [[CrossRef](#)]
7. Luu, P.T.; Lee, J.Y.; Kim, J.W.; Chun, Y.D.; Oh, H.S. Effect of axial-layered permanent-magnet on operating temperature in outer rotor machine. *J. Electr. Eng. Technol.* **2018**, *13*, 2329–2334.
8. Luu, P.T.; Lee, J.; Lee, J.; Park, J. Electromagnetic and thermal analysis of permanent-magnet synchronous motors for cooperative robot applications. *IEEE Trans. Magn.* **2020**, *56*, 1–4. [[CrossRef](#)]
9. Joo, D.; Cho, J.; Woo, K.; Kim, B.; Kim, D. Electromagnetic field and thermal linked analysis of interior permanent-magnet synchronous motor for agricultural electric vehicle. *IEEE Trans. Magn.* **2011**, *47*, 4242–4245. [[CrossRef](#)]
10. Fan, J.; Zhang, C.; Wang, Z.; Dong, Y.; Nino, C.E.; Tariq, A.R.; Strangas, E.G. Thermal analysis of permanent magnet motor for the electric vehicle application considering driving duty cycle. *IEEE Trans. Magn.* **2010**, *46*, 2493–2496. [[CrossRef](#)]
11. Yeo, H.; Park, H.; Seo, J.; Jung, S.; Ro, J.; Jung, H. Electromagnetic and thermal analysis of a surface-mounted permanent-magnet motor with overhang structure. *IEEE Trans. Magn.* **2017**, *53*, 1–4. [[CrossRef](#)]
12. Zhao, N.; Liu, W. Loss calculation and thermal analysis of surface-mounted pm motor and interior PM motor. *IEEE Trans. Magn.* **2015**, *51*, 1–4.
13. Lee, J.; Yeo, H.; Jung, H.; Kim, T.; Ro, J. Electromagnetic and thermal analysis and design of a novel-structured surface-mounted permanent magnet motor with high-power-density. *IET Electr. Power Appl.* **2019**, *13*, 472–478. [[CrossRef](#)]

14. Zhou, K.; Pries, J.; Hofmann, H. Computationally efficient 3-D finite-element-based dynamic thermal models of electric machines. *IEEE Trans. Transp. Electrification* **2015**, *1*, 138–149. [[CrossRef](#)]
15. Marignetti, F.; Delli Colli, V.; Coia, Y. Design of axial flux PM synchronous machines through 3-D coupled electromagnetic thermal and fluid-dynamical finite-element Analysis. *IEEE Transac. Ind. Elec.* **2008**, *55*, 3591–3601. [[CrossRef](#)]
16. Zhang, Y.; McLoone, S.; Cao, W.; Qiu, F.; Gerada, C. Power loss and thermal analysis of a MW high-speed permanent magnet synchronous machine. *IEEE Trans. Ener. Conv.* **2017**, *32*, 1468–1478. [[CrossRef](#)]
17. Dong, J.; Huang, Y.; Jin, L.; Lin, H.; Yang, H. Thermal optimization of a high-speed permanent magnet motor. *IEEE Trans. Magn.* **2014**, *50*, 749–752. [[CrossRef](#)]
18. Koronides, A.; Krasopoulos, C.; Tsiakos, D.; Pechlivanidou, M.S.; Kladas, A. Particular coupled electromagnetic, thermal, mechanical design of high-speed permanent-magnet motor. *IEEE Trans. Magn.* **2020**, *56*, 1–5. [[CrossRef](#)]
19. Kolondzovski, Z.; Arkkio, A.; Larjola, J.; Sallinen, P. Power limits of high-speed permanent-magnet electrical machines for compressor applications. *IEEE Trans. Ener. Conv.* **2011**, *26*, 73–82. [[CrossRef](#)]
20. Bianchi, N.; Bolognani, S.; Frare, P. Design criteria for high-efficiency SPM synchronous motors. *IEEE Trans. Ener. Conv.* **2006**, *21*, 396–404. [[CrossRef](#)]
21. Lee, J.-Y.; Kang, D.-H.; Chang, J.-H.; Hong, J.-P. Rapid eddy current loss calculation for transverse flux linear motor. *Proc. IEEE Ind. Appl. Annu. Meeting* **2006**, *1*, 400–406.



© 2020 by the authors. Licensee MDPI, Basel, Switzerland. This article is an open access article distributed under the terms and conditions of the Creative Commons Attribution (CC BY) license (<http://creativecommons.org/licenses/by/4.0/>).